



ELSEVIER

Tectonophysics 320 (2000) 17–29

TECTONOPHYSICS

www.elsevier.com/locate/tecto

Active deformation in the inner western Alps inferred from comparison between 1972-classical and 1996-GPS geodetic surveys

Christian Sue^{a, b, *}, Joseph Martinod^a, Pierre Tricart^b, François Thouvenot^a, Jean-François Gamond^a, Julien Fréchet^a, Delphine Marinier^a, Jean-Paul Glot^a, Jean-Robert Grasso^a

^a *Laboratoire de Géophysique Interne et Tectonophysique, Observatoire de Grenoble, UMR CNRS 5559, BP53, F-38041 Grenoble cedex 9, France*

^b *Laboratoire de Géodynamique des Chaînes Alpines, UPRES-A CNRS 129, 15 rue M. Gignoux, F-38000 Grenoble, France*

Received 23 December 1998; accepted for publication 7 January 2000

Abstract

Eighteen geodetic points surveyed in 1972 by the French National Geographic Institute (IGN) were remeasured by GPS in 1996 in the Briançonnais and Piémont Zones, east of the Pelvoux massif (French Western Alps). A displacement vector set was determined for the two surveys' common points. Calculations of the strain-rate tensors associated with 15 triangular cells of the network have been performed. Only four of them show a strain rate significant at a 95% level of confidence. These data suggest an E–W extension of about 2–4 mm/yr between the western and eastern part of the network (Pelvoux external crystalline massif and Queyras blueschists, respectively) associated with N–S shortening. This active deformation agrees with neotectonic and seismotectonic data. The measured tectonic motion seems to be distributed throughout the central part of the Briançonnais zone, where the seismic activity is concentrated. The local seismicity has been precisely surveyed since 1989. It is moderate ($M_1 < 4.7$) and no larger earthquake occurred in the 1972–1989 period. The seismic deformation of the 1972–1996 period, extrapolated from the 1989–1996 local seismicity, accounts for less than 10% of the geodetic deformation. Thus, aseismic processes accommodated more than 90% of the observed deformation during this period. This could correspond to accumulation of elastic strain on locked faults, creep on faults or plastic deformation in a large crustal volume. © 2000 Elsevier Science B.V. All rights reserved.

Keywords: active tectonics; Alps; Briançonnais Zone; geodesy; normal faulting; seismicity

* Corresponding author. Present address: Institut de géologie, Rue E. Argand, 11, 2007 Neuchâtel, Switzerland.
Tel.: +41-32-918-26-53; fax: +41-32-918-26-01.

E-mail address: christian.sue@geol.unine.ch (C. Sue)

1. Geological and tectonic framework

The Briançonnais area has been known for 50 years to be the most active seismic zone in the Western French Alps (e.g. Rothé, 1941; Fréchet and Pavoni, 1979). As a whole, the Alpine collision belt undergoes moderate shortening in response to the rather low Europe–Africa convergence rate (less than 1 cm/yr; DeMets et al., 1990). Field tectonic analysis recently provided evidence that the Briançonnais area could undergo neotectonic activity in agreement with the present-day regional seismicity (Sue et al., 1997; Sue, 1998). To test this hypothesis on a shorter time scale, a geodetic measurement campaign was organised in this region during the summer of 1996 (Fig. 1). Eighteen monuments were remeasured by GPS, previously measured in 1972 using laser-ranging and triangulation (Fig. 2).

The remeasured network extends NW–SE, oblique to the Alpine structures that roughly trend NNW–SSE in this part of the Western Alps arc (Fig. 1). Its NW tip is located at the western side of the Pelvoux massif that corresponds to the innermost part of the external Alpine zone (Dauphiné Zone). The network straddles the Briançonnais Zone, its SE tip being located in the Piémont Zone in the Queyras region (Fig. 2). The Briançonnais and Piémont internal Alpine nappes were thrust during Eocene times under high-pressure and low-temperature metamorphic conditions, the whole structure being subsequently thrust westward onto the present day external zone during Late Oligocene times (Tricart, 1984). During the Miocene, a third schistosity-associated deformation accompanied the eastward back-thrusting of the whole nappe pile, as a last expression of the Alpine shortening in this region (Tricart, 1984).

To the east of the Briançonnais frontal thrust (thick line on figures) the metamorphic nappe pile subsequently underwent brittle extension which resulted in the development of dense networks of normal faulting in the Briançonnais (Virloviet et al., 1996) and Queyras zones (Lazarre et al., 1994). This Late Alpine dense fault network developed at a regional scale along two major trends (Barfély et al., 1968; Sue et al., 1997 and Fig. 2):

(1) longitudinal to the main Alpine structures, N140E–N160E, with a major fault located in the hanging wall of the Briançonnais frontal thrust and probably rooting into it at depth (Tricart et al., 1996; Sue and Tricart, 1999); (2) transverse to the Alpine structures, N50E–N80E. Along each trend, fracturing resulted in multiscale conjugate normal faults, ranging from faulted zones a few kilometres wide to dense joint sets. Cross-cutting relationships indicate that both faults families developed simultaneously. Nevertheless, down-throw is greater along longitudinal faults, the dominant relative movement being a collapse of the eastern block, with subsequent strike-slip dextral movement (Sue et al., 1997). These strike-slip motions always post-date normal faulting, as already described by Labaume et al. (1989) in the Digne nappe, south of the studied area.

Tectonic data characterize a transtensive tectonic regime, to the east of the Pelvoux Massif, governed by extensional–dextral motion along N160° longitudinal faults (Sue et al., 1997; Sue, 1998; Sue and Tricart, 1999). Overprinting all compressional ductile Alpine structures, this Late-Alpine (probably recent) extension phase remains undated (Tricart et al., 1996). Geological conditions are not favourable for the observation of active faults because of significant glacial erosion during the Würm period, and the presence of dense forests and active landslides in the region. Recent and ongoing neotectonic and seismotectonic investigations suggest that this extension, combined with dextral strike-slip along the Alpine arc, could still be active (Sue et al., 1997; Sue, 1998). The 1996 geodetic measurements were carried out to check this hypothesis.

2. Geodetic data

During the Summer of 1996, the positions of 18 monuments installed and surveyed in 1972 by the French ‘Institut Géographique National’ (IGN) were remeasured using GPS. The ‘Briançonnais 1972’ campaign gave the positions of 130 monuments by means of 712 angle measurements, and three laser-ranging profiles along the Guisane, Guil and Vallouise valleys (Fig. 2) made of 25 distance measurements. The standard devia-

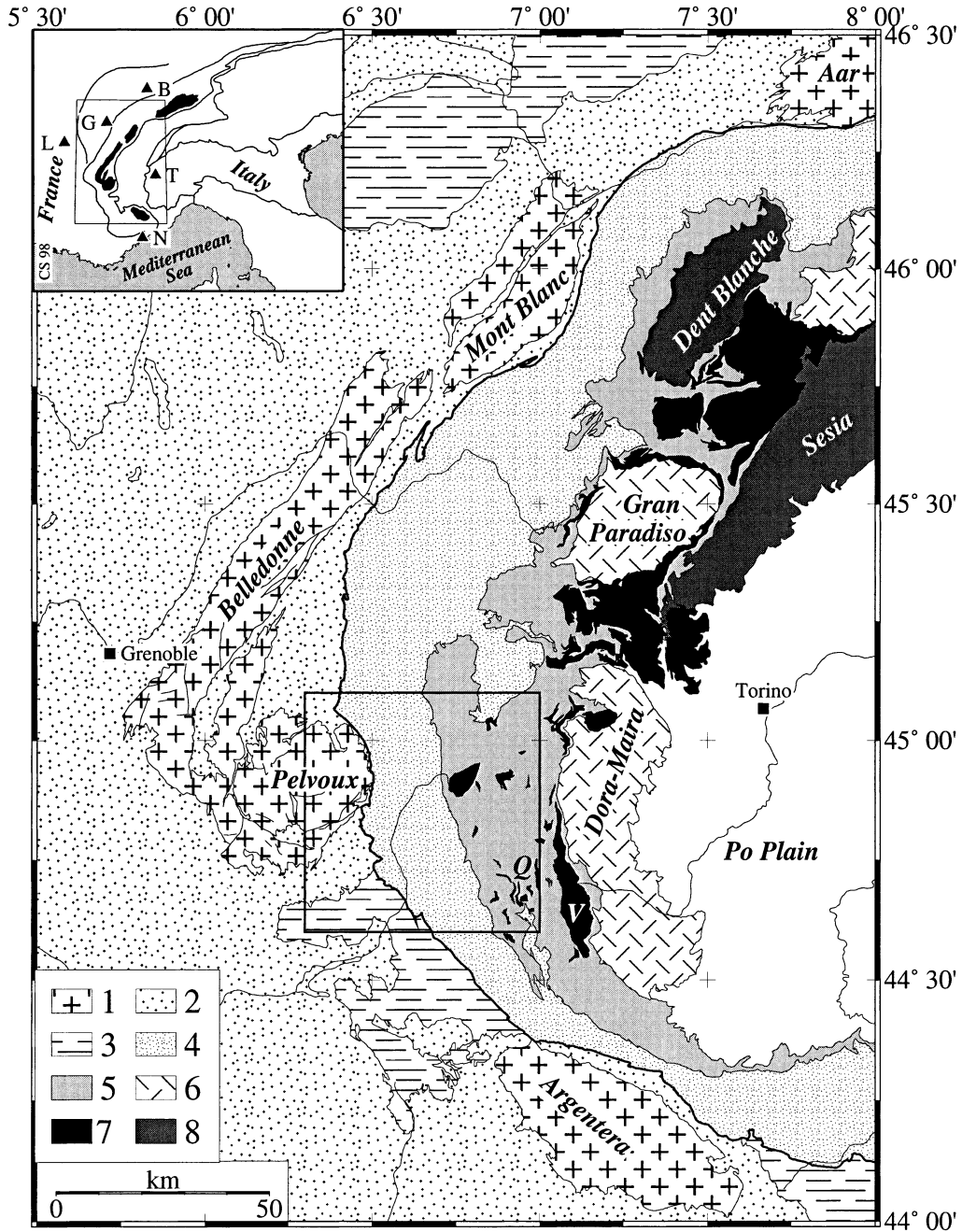


Fig. 1. Location map of the studied area in the western Alps. The boxed shows the area covered by the geodetic network, from the Pelvoux massif to the Queyras region. (1) External Crystalline Massifs (ECM), Dauphiné Zone; (2) Meso-Cenozoic sedimentary cover of the ECM, Dauphiné Zone; (3) Prealpes and Exotic flysch nappes; (4) Briançonnais, Subbriançonnais and Valais Zones; (5) metasediments of the Piémont Zone; (6) Internal Crystalline Massifs; (7) main ophiolites of Piémont Zone; (8) Austro-Alpines nappes. Towns: B: Bern; G: Genève; L: Lyon; N: Nice; T: Torino. Massifs: Q: Queyras; V: Viso. The thick line represents the frontal thrust of the internal metamorphic nappes onto the External Zone.

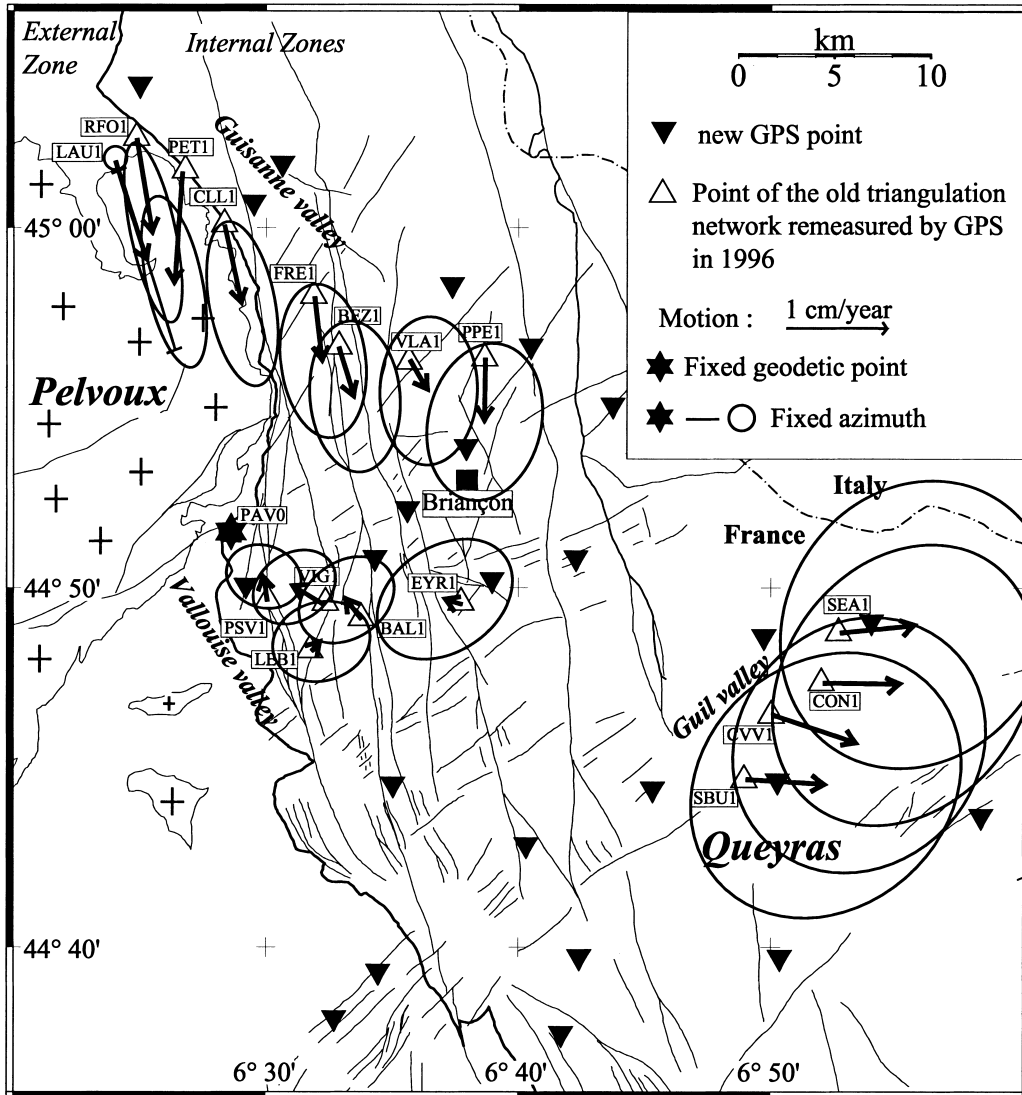


Fig. 2. Displacements of the 1972–1996 common geodetic points. Displacements of the common points and corresponding 95% confidence ellipses, computed assuming that the PAV0 point remained fixed, and that the LAU1-PAV0 azimuth did not change between 1972 and 1996.

tion of the horizontal angle measurements, σ_v , is assumed to be:

$$\sigma_v = \sqrt{k(A/D)^2 + (B/\sqrt{n})^2} \quad (1)$$

where σ_v is expressed in 10^{-4° , D is the distance (km), n the number of repeats of the measurements, A (20 mm) and B ($6.3 \times 10^{-4^\circ}$ for T3, $7.6 \times 10^{-4^\circ}$ for T2 Wild theodolites) are the standard deviations

of the centring and the instrumental error, respectively, and $k=0.3283$ is a conversion factor (values derived from the adjustments of the conventional survey according to IGN studies).

The standard deviation of the distance measurement, σ_d , is given by:

$$\sigma_d = \sqrt{a^2 + b^2 D^2} \quad (2)$$

where σ_d is expressed in metres, D is the distance (m), and a (2×10^{-2} m) and b (5×10^{-6}) are two coefficients associated with the instrument type (AGA 8; standard manufacturer's values). These manufacturer's values may underestimate the uncertainty. Nevertheless, the small distances measured (typically 2 km) result in an important relative uncertainty because of the 'a' factor of (2). Thus, the distance measurements are only useful to determine the scale of the old network *as a whole*, the distance being combined with angle measurements. Because of their low relative accuracy, they do not improve the accuracy of the old network. As a consequence, the distance between two points in the same valley is not better constrained than the distance between two points that are only linked by angle measurements.

The GPS network measured in 1996 consists of 27 first-order points. Most of them are new points installed in 1996 to be remeasured in the future (black triangles on Fig. 2). They were measured in at least three 12 h night-sessions using Ashtech Z-XII receivers. We also looked for the 1972 monuments and checked them. Stability and accessibility problems account for the shape of the measured network, as the monuments are mainly located along reachable valleys. Eighteen 1972 monuments (second-order points; white triangles on Fig. 2) were remeasured in three 8 h day sessions. Two complementary points (PPE1 and EYR1) were measured for 2 h during the fall of 1996. GPPS and GEOLAB software was used to process the data and adjust them, respectively. The accuracy of new GPS data is much better than that of the old conventional data. Therefore, the 95% confidence ellipses calculated for the point motion are mostly a consequence of the uncertainties associated with the old data. We assigned a constant elevation of 53.6 m for the geoid above the WGS84 reference ellipsoid. This elevation was deduced from the comparison between the ellipsoidal and orthometric height of the points of the network. Orthometric heights are the IGN values (derived from levelling and vertical triangulation) and ellipsoidal heights are the GPS-related heights of the network points based on the IGS network. This comparison shows that the geoid is roughly parallel to the ellipsoid in the Briançonnais area.

3. Displacement field

Two sets of independent coordinates for both the IGN triangulation survey and the GPS survey have been computed to compare the position of the 1972 and 1996 networks. Since neither the absolute position nor the orientation of the old network is precisely known, we have to fix the position of one point and one azimuth (black star and white circles on Fig. 2, respectively) to compare 1972 and 1996 data. Because of distance measurements, the size of the old network is known, and *no scale factor* has to be taken into account. Therefore, the size and shape of the two networks can be compared, but they can translate (fixed-point hypothesis) and rotate (fixed azimuth hypothesis) with respect to each other. Finally, the calculated motions may result from tectonics, landslides (or other local phenomena), measurement errors, and also from a translation and/or a rigid rotation of the network induced by our fixed-point/azimuth choices.

Fig. 2 presents the displacement field, with its corresponding 95% confidence ellipses, calculated assuming that point PAV0 is fixed and that no variation in the LAU1-PAV0 azimuth occurred between 1972 and 1996. Table 1 lists the parameter set for this displacement field. We obtain roughly 10 mm/yr motion toward the south for the points located in the Guisane Valley, and toward the east for the points located in Queyras. Much slower displacements could also fit our data because of the large uncertainties on the 1972 coordinates. These motions appear rapid regarding boundary conditions of the Alpine collision belt (Europe–Africa convergence; DeMets et al., 1990). Anyway, we cannot draw tectonic conclusions because of the large uncertainties that are partly linked to the fixed point and azimuth choices. These choices can also imply a possible global rotation of the network. To eliminate these problems, in the next section, we extract the parameters of the displacement field that are independent of any a priori fixed hypothesis.

4. Strain-rate tensor calculations and Monte-Carlo analysis

To eliminate the unconstrained parameters, we extract the symmetrical part of the deformation-

Table 1

Absolute displacements and 95% confidence domains plotted on Fig. 1 (PAV0 position and LAU1-PAV0 azimuth fixed)

Point code	IGN name	Local name	Latitude	Longitude	Orthometric altitude	Δx (mm)	Δy (mm)	$e1$ (mm)	$\alpha e1$ (°)	$e2$ (mm)
BAL1	St. Martin de Queyrière IV	La Balmette	44°49'00"	6°33'49"	1349	43	−52	134	53	99
BEZ1	La Salle II	Le Bez	44°56'37"	6°33'05"	1450	−41	117	195	173	117
CLL1	Le Monetier IX	Clot Laroche	45°00'04"	6°28'40"	1708	−49	193	215	167	85
CON1	Aiguille I	La Condamine	44°46'58"	6°51'57"	1564	−192	−4	390	35	310
CVV1	Château Ville Vieille VI	La Pissarote	44°46'06"	6°49'56"	1468	−213	63	347	41	310
EYR1	Villrd St. Pancrace I	Peyre Eyraute	44°49'22"	6°37'48"	2946	33	−8	191	54	136
FRE1	Le Monetier XIII	Le Freyssinet	44°58'02"	6°32'11"	1480	−24	158	199	171	110
LAU1	Villard d'Arène IV	Col du Lautaret	45°01'53"	6°24'23"	2136	−87	244	240	163	0
LEB1	L'Argentière la Bessée	Château Lebrun	44°48'08"	6°31'49"	2123	−18	−17	128	72	102
PAV0	Vallouise II	Pas d'Aval	44°51'28"	6°28'44"	1634	−	−	−	−	−
PET1	Le Monetier VII	Petit Etret	45°01'34"	6°27'02"	1790	1	279	225	166	72
PPE1	Val des Prés II	Petite Peyrolle	44°56'14"	6°38'52"	2656	−3	154	205	11	147
PSV1	Puy St. Vincent II	Les Prés	44°49'33"	6°30'07"	1407	9	−56	99	108	80
RFO1	Le Monetier II	Roche Fournière	45°02'31"	6°25'14"	1988	−47	230	236	166	58
SBU1	Château Ville Vieille IV	Sommet Bucher	44°44'18"	6°48'50"	2276	−197	5	374	47	317
SEA1	Aiguille	Serre de l'Aigle	44°48'21"	6°52'40"	2496	−187	−25	386	32	339
VIG1	Les Vigneaux II	Les Vigneaux	44°49'25"	6°32'21"	1113	74	−42	114	55	87
VLA1	St. Chaffrey I	Villard Laté	44°56'13"	6°35'54"	1562	−43	69	191	180	126

Δx and Δy are the displacement components, $\alpha e1$ is the azimuth of the major axis of the 95% confidence ellipses, $e1$ and $e2$ are the values of the semi-major and semi-minor axes, respectively.

rate tensor. The Briançon area was discretised in triangular cells formed by sets of three neighbouring points of the network. Assuming that deformation is continuous within each cell, we calculated the deformation-rate tensor:

$$(\dot{d}_{ij}) = \begin{bmatrix} \dot{d}_{EE} & \dot{d}_{NE} \\ \dot{d}_{EN} & \dot{d}_{NN} \end{bmatrix}, \quad (3)$$

where E and N refer to the E–W and N–S axis, respectively. To calculate this tensor, we use a displacement field, i.e. we must choose a fixed azimuth (for instance, we used the displacement field presented in Fig. 2 and Table 1). However, the symmetrical part of this tensor, the strain-rate tensor, does not depend on any rigid rotation, i.e. of an a priori fixed choice of the azimuth.

Table 2 gives the parameters of the strain-rate tensors for 15 triangular cells of the network. We give $\dot{\gamma}_1 = \dot{\epsilon}_{EE} - \dot{\epsilon}_{NN}$, $\dot{\gamma}_2 = 2\dot{\epsilon}_{EN}$ and $\dot{\delta} = \dot{\epsilon}_{EE} + \dot{\epsilon}_{NN}$ with their standard deviations, and $\dot{I} = \sqrt{(\dot{\gamma}_1^2 + \dot{\gamma}_2^2)}$. $\dot{\gamma}_1$ measures the angle variations between the SE–NW and NE–SW axis, while $\dot{\gamma}_2$ measures the angle variations between the N–S and E–W axis (Franck, 1966; see also Feigl et al., 1990). \dot{I}

quantifies the shear of the cell, while $\dot{\delta}$ is the dilatation of the triangular cell that can be determined using the distance measurements of the old data. Table 2 also gives the eigenvalues λ_1 and λ_2 of the strain tensor (maximum extension and shortening, respectively), the azimuth of the extensional axis, and the rigid rotation $\dot{\omega}$ of the cell. Note that except for $\dot{\omega}$, all these parameters are independent of any fixed azimuth choice. $\dot{\omega}$ is reported in Table 2 because the difference in rigid rotation between two cells is not a function of the fixed azimuth, i.e. it is constrained by the data. The principal axes of the strain-rate tensors are presented on Fig. 3 by red (for shortening) or green (for extension) bars whose length is proportional to the strain tensor eigenvalues.

A Monte-Carlo analysis based on a Gaussian distribution was performed in order to evaluate the uncertainty of these strain-rate tensors. Eighty perturbed strain-rate tensors were calculated for each triangular cell, with different randomly perturbed initial coordinates taking into account the correlation between positions derived from geodetic measurement (i.e. taking into account the

Table 2
Parameters and principal axes of the strain-rate tensors plotted on Fig. 3

Triangle	Az(λ_1)	λ_1	$\sigma(\lambda_1)$	λ_2	$\sigma(\lambda_2)$	δ	$\sigma(\delta)$	$\dot{\gamma}_1$	$\sigma(\dot{\gamma}_1)$	$\dot{\gamma}_2$	$\sigma(\dot{\gamma}_2)$	$\dot{\omega}$	$\sigma(\dot{\omega})$	\dot{I}	$\sigma(\dot{I})$
RFO1-LAU1-CLL1	167.7	0.13	0.38	-0.71	0.39	-0.58	0.65	-0.77	0.49	-0.35	0.66	-14.8	12.1	0.85	0.41
LAU1-BEZ1-PAV0	77.9	0.01	0.22	-0.52	0.17	-0.51	0.25	0.48	0.28	0.21	0.36	21.9	8.0	0.52	0.30
FRE1-PPE1-BEZ1	114.9	-0.08	0.21	-0.90	0.44	-0.98	0.51	0.53	0.49	-0.63	0.47	13.0	14.7	0.82	0.47
BEZ-PAV0-VLA1	71.6	0.14	0.21	-0.79	0.35	-0.65	0.39	0.74	0.45	0.56	0.52	10.1	12.7	0.93	0.43
BAL1-VLA1-PAV0	64.8	0.00	0.19	-0.45	0.21	-0.45	0.25	0.29	0.37	0.34	0.37	23.5	7.0	0.45	0.32
VIG1-PSV1-PAV0	141.5	-0.51	0.29	-1.14	0.33	-1.65	0.43	-0.14	0.75	-0.62	0.52	11.3	19.5	0.64	0.46
PSV1-VIG1-LEB1	156.9	0.79	0.53	-1.23	0.33	-0.44	0.67	-1.4	0.58	-1.46	0.64	-14.5	14.8	2.02	0.58
LEB1-VIG1-BAL1	141.5	0.85	0.55	-0.41	0.37	0.45	0.67	-0.28	0.62	-1.22	0.83	-35.3	10.4	1.25	0.66
PPE1-VLA1-BAL1	146.2	-0.05	0.38	-0.63	0.21	-0.68	0.38	-0.22	0.45	-0.54	0.7	51.9	16.4	0.58	0.49
EYR1-PPE1-BAL1	96.9	0.06	0.21	-0.50	0.16	-0.44	0.19	0.55	0.38	-0.14	0.47	27.9	12.1	0.57	0.33
SBU1-EYR1-LEB1	133.2	0.54	0.32	-0.47	0.33	0.07	0.44	0.06	0.50	-1.00	0.52	-8.7	7.1	1.00	0.47
CVV1-SBU1-EYR1	99.2	0.63	0.30	-0.57	0.34	0.06	0.37	1.14	0.53	-0.38	0.73	27.1	13.0	1.20	0.52
PPE1-EYR1-CVV1	96.6	0.65	0.27	-0.51	0.19	0.14	0.24	1.12	0.38	-0.26	0.48	29.6	4.9	1.15	0.40
SEA1-CVV1-PPE1	26.1	0.39	0.24	0.07	0.21	0.46	0.25	-0.20	0.50	0.25	0.51	-9.9	7.9	0.32	0.37
CON1-SEA1-CVV1	36.5	0.38	0.47	-0.73	0.94	-0.35	1.20	-0.33	1.01	1.06	1.16	-12.2	23.5	1.11	0.88

Az(λ_1), λ_1 and λ_2 are, respectively, the azimuth of the principal extensional axis and the values of the major and minor axes of the tensors (in 10^{-6} /yr). $\dot{\gamma}_1$, $\dot{\gamma}_2$, \dot{I} , δ represent the parameters independent of any fixed-azimuth choice defined in the text (in microradian/yr). $\dot{\omega}$ is the rigid rotation of the cells in 10^{-6} /yr. Statistically significant $\dot{\gamma}_1$ and $\dot{\gamma}_2$ parameters at a 95% level of confidence are shown in bold.

full information of the variance/covariance matrix). The dispersion obtained for the eigenvalues and eigenvectors of the strain-rate tensors is represented on Fig. 3 by the clusters of points. This method enables an evaluation of the 95% confidence domains of the strain-rate tensors (Kasser et al., 1987).

Among the 15 cells of the discretisation, six provide parameters linear with (ϵ_{ij}) and independent of any choice ($\dot{\gamma}_1$, $\dot{\gamma}_2$ or δ) larger than their 95% confidence value. Three parameters concern dilatation and have negative values (LAU1-BEZ1-PAV0, VIG1-PSV1-PAV0, EYR1-PPE1-BAL1 cells) meaning that the area of the cells decreased between 1972 and 1996. We also observe that the PSV1-VIG1-LEB1 cell exhibits very large $\dot{\gamma}_1$ and $\dot{\gamma}_2$ values. The deformation of this cell may result from a local motion to the NE of the PSV1 point. This would also explain the high δ value of the VIG1-PSV1-PAV0 cell. Since this point is located at the southern margin of the network, it is not possible to demonstrate conclusively that this motion is anomalous. We conclude that both the VIG1-PSV1-PAV0 and the PSV1-VIG1-LEB1 cells show that the PSV1 point moved significantly, at least 4.5 cm to the NE between 1972 and 1996

(Table 2). We suspect, however, that this motion results from a local instability and not from the tectonic activity of the region, so we removed all PSV1-related data.

Significant negative δ values are observed in two other cells, LAU1-BEZ1-PAV0 and EYR1-PPE1-BAL1, which stand between the Guisane and Vallouise valleys, with no direct distance measurement between them. They can be interpreted in term of tectonic motions. Such negative δ values do not necessarily imply that thrusting occurred within these cells. For instance, the negative dilatation of the EYR1-PPE1-BAL1 cell probably results from dextral strike-slip faulting along the numerous N160E longitudinal faults that are clearly visible in the field (Fig. 1). The other δ values are often negative, within their 95% confidence ellipses, except for the cells located east of Briançon where δ is positive, although it is always within the 95% confidence ellipses. Note that several high \dot{I} values suggest that strike-slip faulting occurs within the network as a whole.

Finally, two cells located in the eastern part of the network (CVV1-SBU1-EYR1, PPE1-EYR1-CVV1) provide $\dot{\gamma}_1$ values greater than their 95% confidence value and significant strain-rate tensors

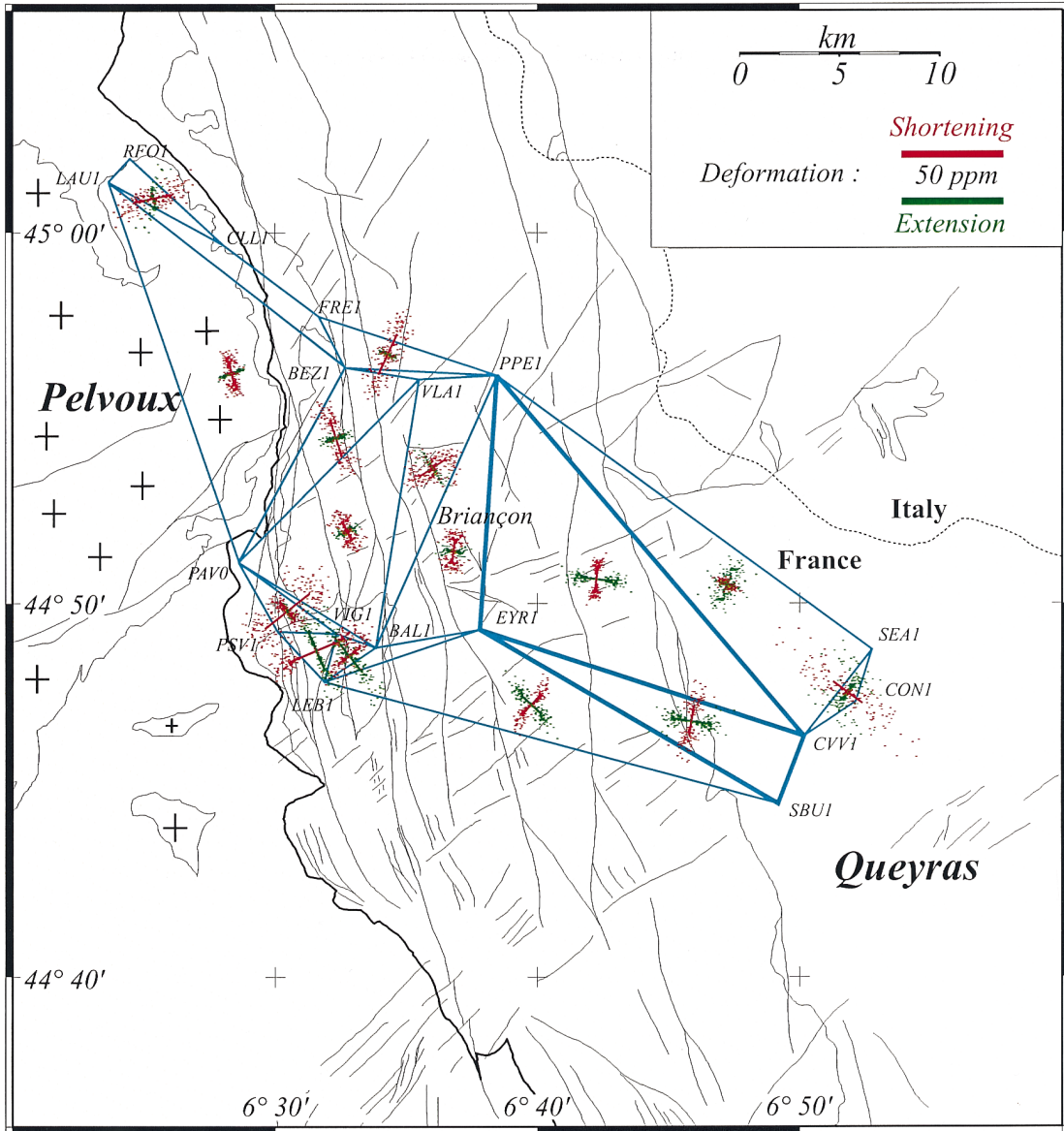


Fig. 3. Strain rate tensors. Principal axes of the strain-rate tensor computed for each triangular cell. Red and green bars represent the shortening and extension directions, respectively. Clusters of points at the end of bars represent the dispersion of the data as computed by a Monte-Carlo analysis. Thick blue lines outline the triangular cells, which provided significant $\dot{\gamma}_1$ and $\dot{\gamma}_2$ deformation parameters at a 95% level of confidence (see also figures shown in bold in Table 2).

(Fig. 3 and Table 2). The cell SBUI-EYR1-LEB1 in the same area provides a $\dot{\gamma}_2$ value significant at a 94.6% confidence level and strain-rate tensors consistent with the CVV1-SBUI-EYR1 and PPE1-EYR1-CVV1 ones. These three cells exhibit

E–W to NW–SE extension combined with N–S to NE–SW shortening. These deformations cannot be suspected to result from the instability of a monument of the network. As a matter of fact, although EYR1 is a common point of these cells,

it does not move abnormally with respect to the points located in the western part of the network. Thus, the roughly E–W extension evidenced in these three cells does not result from an anomalous westward motion of this point. Moreover, the strain-rate tensors of the three cells SBU1-EYR1-LEB1, CVV1-SBU1-EYR1 and PPE1-EYR1-CVV1 present a good internal coherency

and are consistent with the extensional and strike-slip focal mechanisms of Fig. 4.

The statistically significant $\dot{\gamma}_1$ values at a 95% level of confidence are shown in bold in Table 2 (except for the cells including point PSV1, as explained above), while the thick lines of Fig. 3 show the corresponding triangular cells. The CVV1-SBU1-EYR1 and PPE1-EYR1-CVV1 also

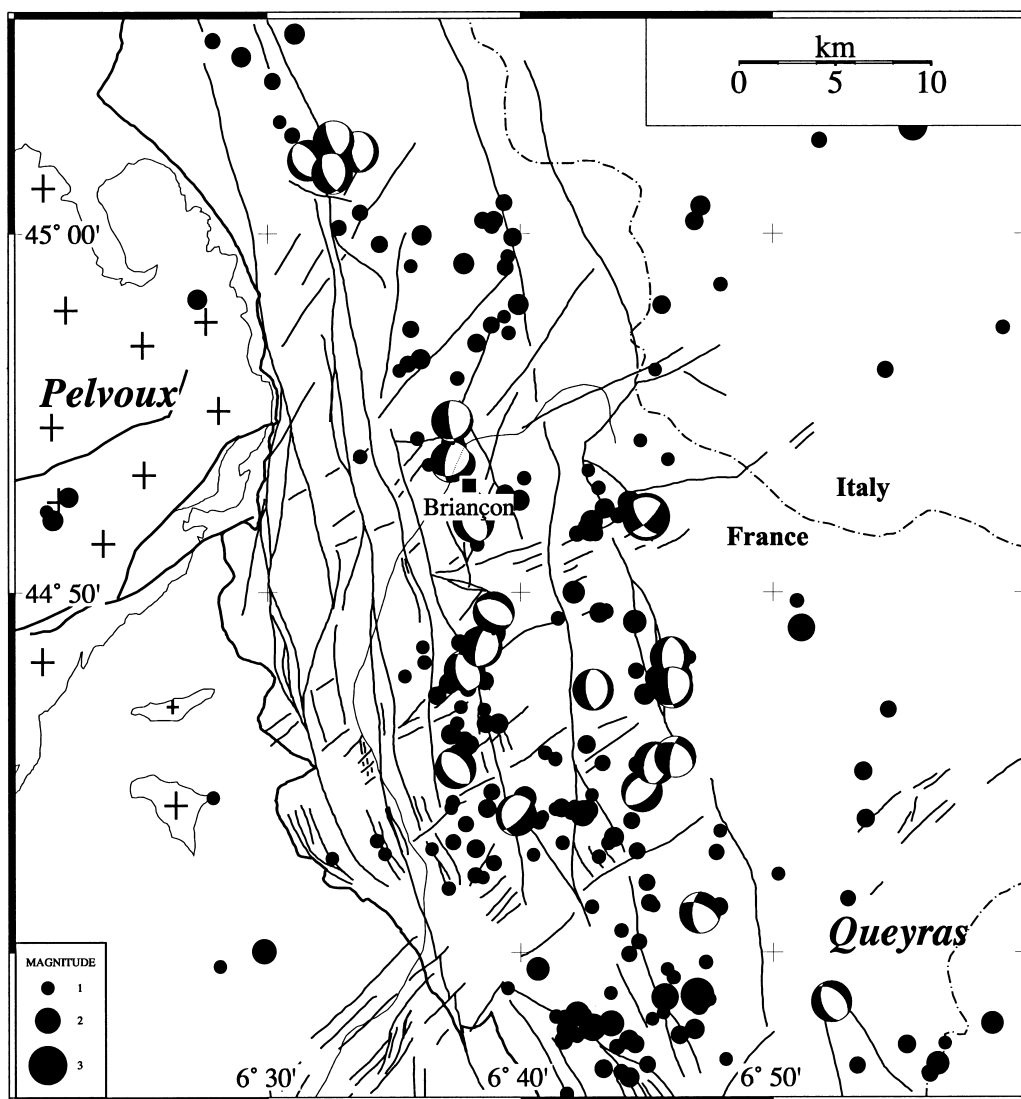


Fig. 4. Seismotectonics. Earthquakes epicenters for the period 1989/1996 (only local magnitude M_L greater than 1) with reliable focal mechanisms. Present-day tectonic deformation is extensional to transtensional across the Briançonnais zone. The map also shows the fault network, which post-dates the alpine shortening and is characterized by normal to transcurrent kinematics (deduced from aerial photography interpretation and field analysis).

provide significant λ_1 and λ_2 parameters at a 95% level of confidence, which only concerns the length of the strain axes and not their orientations. Deformation velocities can be estimated with these reliable data, e.g. for the PPE1-EYR1-CVV1 cell. For this cell, $\dot{\gamma}_1 = 1.12$ microradian/yr with a standard deviation of 0.38; $\lambda_1 = 0.65 \times 10^{-6}$ /yr with a standard deviation of 0.27 and $\lambda_2 = -0.51 \times 10^{-6}$ /yr with a standard deviation of 0.19. Then, we obtain a *minimum* $\dot{\gamma}_1$ value of 0.38 microradian/yr; a λ_1 value of 0.12×10^{-6} /yr and a λ_2 value of -0.14×10^{-6} /yr at a 95% level of confidence. If we multiply these deformation rates by the characteristic length of the triangular cell, roughly 15 km, we obtain minimum velocities of 1.8 mm/yr for the E–W extension and 2.1 mm/yr for the N–S shortening at a 95% level of confidence.

The CVV1-SBU1-EYR1 cell also deformed significantly between 1972 and 1996. Although the minimum velocities that are required by the corresponding strain-rate tensor are smaller than for the PPE1-EYR1-CVV1 cell, the strain-rate tensors are consistent with tectonic velocities as high as 4 mm/yr.

In conclusion, the analysis of the deformation of these two triangular cells situated in the eastern part of the network suggests tectonic deformation combining N–S shortening and E–W extension at a velocity ranging from 2 to 4 mm/yr.

5. Discussion and conclusion: rapid tectonic motions in the Briançonnais Zone

The comparison between the 1972 and 1996 data shows that the geodetic network deformed significantly during the past 24 years in the eastern part of the studied area, whereas most of the observed deformation in the western and central part of the network is not statistically significant at a 95% level of confidence. Geodesy indicates that deformation concentrates along the eastern part of the Briançonnais Zone, where the seismicity is located (Fig. 4). Statistically significant strain-rate tensors indicate an active E–W extensional tectonic regime, associated with N–S shortening with velocities of several mm/yr.

The studied area belongs to the Briançonnais seismic arc, the most active seismic zone of SE France (e.g. Rothé, 1941; Sue, 1998; Sue et al., 1999). Fig. 4 shows earthquakes located by the Sismalp seismological network (Thouvenot et al., 1990) during the 1989/1996 period. Earthquakes were located using HYPREF, an improved version of the HYPO71 program (Lee and Lahr, 1975); focal mechanisms were computed with the FPFIT software (Raesenberg and Oppenheimer, 1985). In Fig. 4, only earthquakes with a number of observations larger than 10, a M_1 magnitude larger than 1 and a *r.m.s.* (misfit to the picked arrival time for the Pg phases) less than 0.5 s were selected; moreover, only reliable focal mechanisms were retained (at least 10 polarity readings with a fairly homogeneous distribution). The epicentral uncertainty is estimated to be about 1 km.

Seismicity concentrates along a N160E-oriented zone that roughly follows the mapped fault system (Sue, 1998). Most events are located within the upper 10 km of the crust and have a magnitude smaller than 3, except for the Cervières earthquake ($M_1 = 4.7$) and its largest aftershocks ($M_L = 3.8$ and 3.7) (Thouvenot et al. 1991). Focal mechanisms demonstrate a globally extensional tectonic regime all over the eastern part of the Briançonnais area (Fig. 4; Sue, 1998; Sue et al., 1999). Numerous normal-faulting focal mechanisms suggest that the longitudinal fault system accommodates this extension. We also found several strike-slip mechanisms with an extensional component, the northernmost being associated with the Cervières earthquake (Thouvenot et al., 1991). Thus, according to seismological data, the Briançon area, east of the Durance valley, deforms in a transtensive seismotectonic regime, seismic deformation being mainly accommodated by the longitudinal fault system.

The geodetic data indicate E–W extension associated with N–S compression, which suggests mainly a strike-slip tectonic regime, consistent with the strike-slip component shown by focal mechanism data (dextral motion along N160E fault system) and with evidence for recent strike-slip displacements observed in the field (Sue, 1998; Sue and Tricart, 1999). The positive dilatation found to the east of the Briançonnais area could be linked to the extensional part of the deformation

inferred from the seismotectonic analysis. Moreover, the two significant strain-rate tensors, east of the Briançonnais area, show E–W extensional axes coherent with the seismotectonic analysis. Geodetic data are rare in this region and concern only levelling (Fourniguet, 1977). These data are consistent with our results, suggesting rapid motion (several mm/yr) and a collapse of the Briançonnais zone with respect of the external crystalline massifs, which are currently uplifting.

To roughly compare the seismic portion of the deformation with the deformation inferred from geodetic measurements, we calculated the total amount of seismic moment M_0 released by the seismic activity for the instrumented period 1989/1996. This total amount is maximised and only provides a rough estimate of the seismic moment released in this area. The total seismic moment per year (about 10^{15} Nm/yr) is dominated by the $M_1=4.7$ Cervières earthquake and its aftershocks. Since 1972, no other large earthquake occurred in this region, and the seismic activity of the period 1972/1988 is quite similar to the seismic activity of the period 1989/1996 (Fréchet and Thouvenot, 1995). Given the limited length of our earthquake catalogue (1989/1996), we can only draw conclusions on the deformation style for a short period, assuming constant seismic and geodetic deformation rates during the period 1972/1996. To compare the seismic moment to an equivalent geodetic moment inferred from the E–W extensional component of our measurements, we used the relation $M_0 = \mu Sd$, with the upper crust shear modulus $\mu = 33$ GPa, S the area of an assumed N–S-striking, 10 km long (the longitudinal size of the eastern part of the network), 45° E-dipping normal fault cutting across a 10 km thick brittle crust (which is the orientation of most of the smaller faults deduced from focal mechanisms and field analyses), and d the slip on the fault. Depending on the total motion inferred from the geodetic data (2 or 4 mm/yr), we obtain an equivalent geodetic moment between roughly 10^{16} Nm/yr and 2×10^{16} Nm/yr. Thus, under these drastic and very coarse hypotheses, the seismic activity only accounts for around 5–10% of the deformation observed during the last 25 years. The effective shear modulus over decade-long time scale could be lower than the conventional value of

33 GPa we used. This could account for a part of the discrepancy between seismic and geodetic moment rates.

Nevertheless, between 1972 and 1996, east of Briançon, aseismic processes must have accommodated part of the deformation. Martinod et al. (1996) found similar conclusions for other parts of the French Alps in the Grenoble region. At a larger scale, Jackson and McKenzie (1988) also inferred similar ratios between seismic and aseismic deformation process in other mountains belts. This very important difference between seismic and aseismic deformation evaluated for the period 1972–1996 in the region of Briançon can be explained by at least three processes: (1) elastic strain accumulation on a locked fault; (2) creep on several faults; and (3) visco-plastic flow deformation in a large crustal volume. The calculation performed in the previous section is not related to a given process. Its aim was to give an estimation of the seismic and geodetic deformation and thus to compare them using actual numbers. Clearly, this short time-scale comparison cannot resolve whether seismic or aseismic processes will accommodate the deformation *in the long term*, and elastic strain energy may be currently accumulating in this area. This region is carved by a well-developed and still active late-alpine fault network (Fig. 4; Sue, 1998; Sue and Tricart, 1999), which suggests that faults have a major role in its present-day tectonics. Thus, case (3), where plastic deformation affects a global volume of the crust with minor role for faults, could be rejected. In case (1), elastic strain energy is currently accumulating in this area, and will be released in future earthquakes, whereas in case (2), continuous creep on several faults on various scales explain the aseismic portion of the deformation. In fact, with our data, it is not possible to choose between these two processes.

Our investigations demonstrate that the Late Alpine transcurrent tectonic regime is still active at a rapid rate with tectonic velocities higher than 2 mm/yr. Geodetic data are also consistent with the E–W extension inferred from seismotectonics. The key point is to explain this transtensive active tectonics in the internal part of the Alps, a still active collision belt. Longitudinal motion along the belt, associated with the rigid counterclockwise

rotation of the Apulian indenter toward stable Europe (Ménard, 1988; Vialon et al., 1989), could explain the transcurrent part of the deformation. The extensional current tectonics, however, develops at the scale of the belt from the Ubaye massif, west of the Viso massif (Fréchet and Pavoni, 1979; Eva et al., 1997) to the Briançon region (this study) and up to the east of the Mont-Blanc massif, i.e. all along the Briançonnais zone (Maurer et al., 1997; Sue, 1998; Sue et al., 1999). The E–W extension in the Briançon area and in a large portion of the belt could result from deep processes in the lithospheric root of the Western Alps. Only a better knowledge of the lithospheric structure could constrain a dynamic model for the belt. Nevertheless, extension could be related to a possible slab detachment that could induce uplift of the external zone and particularly the external crystalline massifs, as already proposed by Lyon-Caen and Molnar (1989), and a collapse of the adjacent internal zones. In fact, both rotational phenomena and deep gravitational processes could act together to generate the present-day observed tectonics in the core of the western Alpine arc.

Acknowledgements

This study was supported by Joseph Fourier University (Grenoble, France) and by the French national program GéoFrance 3D (contribution number 29). The authors wish to thank M. Bouchon, D. Jault, G. Valensise and an anonymous reviewer for many improvements they brought to the manuscript, and T. Berly, N. Borde, M.-E. Claudel, N. Cotte, J.-F. Coutos, F. Janod, M. Kuntz, Y. Liautier, J. Pellottier, L. Richard and C. Savin for carrying batteries and GPS receivers over summits of this country. We are also grateful to the French Institut National des Sciences de l'Univers and J. Ammann to put the GPS receivers at our disposal.

References

- Barfèty, J.C., Gidon, M., Kerckhove, C., 1968. Sur l'importance des failles longitudinales dans le secteur durancien des Alpes internes françaises. *C. R. Acad. Sci. Paris* 267, 394–397.
- DeMets, C., Gordon, R.G., Argus, D.F., Stein, S., 1990. Current plate motions. *Geophys. J. Int.* 101, 425–478.
- Eva, E., Solarino, S., Eva, C., 1997. Stress tensor orientation derived from fault plane solutions in the southwestern Alps. *J. Geophys. Res.* 102, 8171–8185.
- Feigl, K.L., King, R.W., Jordan, T.H., 1990. Geodetic measurements of tectonic deformation in the Santa Maria fold and thrust belt, California. *J. Geophys. Res.* 95, 2679–2699.
- Fourniguet, J., 1977. Mise en évidence de mouvements néotectoniques actuels verticaux dans le Sud-Est de la France par comparaison de nivellements successifs. In: *Rap. BRGM 77SGN081GEO*, 1–35.
- Franck, F.C., 1966. Deduction of earth strain from survey data. *Bull. Seismol. Soc. Am.* 56, 35–42.
- Fréchet, J., Pavoni, N., 1979. Etude de la sismicité de la zone briançonnaise entre Pelvoux et Argentera (Alpes occidentales) à l'aide d'un réseau de stations portables. *Éclog. Geol. Helv.* 72, 763–779.
- Fréchet, J., Thouvenot, F., 1995. Seismicity of the Western Alps. In: XVIIIe Sémin. europ. Génie parasismique, Lyon, 19–32.
- Jackson, J., McKenzie, D., 1988. The relationship between plate motions and seismic moment tensors, and the rates of active deformation in the Mediterranean and Middle East. *Geophys. J. R. Astron. Soc.* 93, 45–73.
- Kasser, M., Ruegg, J.C., Lesage, P., Ortlieb, L., Pagarete, J., Duch, N., Guerrero, J., Roldan, J., 1987. Geodetic measurement of plate motion across the central Gulf of California. *Geophys. Res. Lett.* 14, 5–8.
- Labaume, P., Ritz, J.F., Philip, H., 1989. Failles normales récentes dans les Alpes sud-occidentales: leurs relations avec la tectonique compressive. *C. R. Acad. Sci. Paris* 308, 1553–1560.
- Lazarre, J., Tricart, P., Villemin, T., 1994. L'extension cassante tardi-orogénique dans les schistes lustrés piémontais du Queyras (Alpes occidentales, France). *C. R. Acad. Sci. Paris* 319, 1415–1421.
- Lee, W.H., Lahr, J.E., 1975. HYPO71: a Computer Program for Determining Hypocenter, Magnitude, and First-motion Pattern of Local Earthquakes. *US Geol. Surv. Open File Report* 75-331. 110 pp.
- Lyon-Caen, H., Molnar, P., 1989. Constraints on the deep structure and dynamic processes beneath the Alps and adjacent regions from an analysis of gravity anomalies. *Geophys. J. Int.* 99, 19–32.
- Martinod, J., Jouanne, F., Taverna, J., Ménard, G., Gamond, J.F., Darmendrail, X., Notter, J.C., Basile, C., 1996. Present-day deformation of the Dauphine (SE France) Alpine and Subalpine massifs. *Geophys. J. Int.* 127, 189–200.
- Maurer, H.R., Burkhard, M., Deichmann, N., Green, A.G., 1997. Active tectonism in the central Alps: contrasting stress regimes north and south of the Rhone Valley. *Terra Nova* 9, 91–94.
- Ménard, G., 1988. Structure et cinématique d'une chaîne de collision: Les Alpes occidentales et centrales. Thèse d'Etat, Grenoble University, France.
- Raesenberg, P.A., Oppenheimer, D., 1985. FPFIT FPLOT and FPPAGE: Fortran Computer Programs for Calculating

- and Displaying Earthquakes Fault-plane Solutions. US Geol. Surv. Open File Rep. 85-739. 109 pp.
- Rothé, J.P., 1941. Les séismes des Alpes françaises en 1938 et la sismicité des Alpes occidentales. *Ann. Inst. Phys. Globe Strasbourg* 3, 1–105.
- Sue, C., Fréchet, J., Thouvenot, F., Tricart, P., 1997. Late orogenic extension in the Briançonnais zone, French Alps: tectonic and seismotectonic approaches. *Terra Nova Abst.* 9, Suppl. 1, 307.
- Sue, C., 1998. Dynamique actuelle et récente des Alpes occidentales internes – Approche structurale et sismologique. Ph.D. thesis, Grenoble University, France.
- Sue, C., Tricart, P., 1999. Late-Alpine brittle extension above the Frontal Pennine Thrust near Briançon, Western Alps. *Éclog. Geol. Helv.* 92, 171–181.
- Sue, C., Thouvenot, F., Fréchet, J., Tricart, P., 1999. Widespread extension in the core of the western Alps revealed by earthquake analysis. *J. Geophys. Res.* 104, B11, 25611–25622.
- Thouvenot, F., Fréchet, J., Guyoton, F., Guiguet, R., Jenatton, L., 1990. SISMALP: an automatic phone-interrogated seismic network for the western Alps. *Cahiers Centre Eur. Géodyn. Séism.* 1, 1–10.
- Thouvenot, F., Fréchet, J., Vialon, P., Guyoton, F., Cattaneo, M., 1991. Les séismes de Cervière (Hautes-Alpes) des 11 et 13 février 1991: un coulissage dextre entre zones piémontaise et Briançonnaise. *C. R. Acad. Sci. Paris* 312, 1617–1623.
- Tricart, P., 1984. From passive margin to continental collision: a tectonic scenario for the western Alps. *Am. J. Sci.* 284, 97–120.
- Tricart, P., Bouillin, J.P., Dick, P., Moutier, L., Xing, C., 1996. Le faisceau de failles de Haute-Durance et le jeu distensif du front Briançonnais au SE du Pelvoux (Alpes occidentales). *C. R. Acad. Sci. Paris* 323, 251–257.
- Vialon, P., Rochette, P., Ménard, G., 1989. Indentation and rotation in the western alpine arc. In: Coward, M.P., Dietrich, D., Park, R.G. (Eds.), *Alpine Tectonics*. Geol. Soc. London, Spec. Publ. 45, 329–338.
- Virlovet, B., Tricart, P., Villemin, T., 1996. Blocs basculés tardoalpins dans les nappes Briançonnaises de Haute-Durance (Alpes occidentales, France) et évolution néotectonique des zones internes. *C. R. Acad. Sci. Paris* 322, 475–481.